Operando space-resolved inhomogeneity in lithium diffusion across NMC and graphite electrodes in cylinder-type Li-ion batteries

Graae, Kristoffer Visti; Li, Xinyu; Etter, Martin; Schökel, Alexander; Norby, Poul

Published in:
Journal of Energy Storage

Link to article, DOI:
10.1016/j.est.2023.109523

Publication date:
2023

Document Version
Publisher's PDF, also known as Version of record

Journal of Energy Storage 74 (2023) 109523

Contents lists available at ScienceDirect

Journal of Energy Storage

journal homepage: www.elsevier.com/locate/est

Research papers

Operando space-resolved inhomogeneity in lithium diffusion across NMC and graphite electrodes in cylinder-type Li-ion batteries

Kristoffer Visti Graae [a,*], Xinyu Li [a], Martin Etter [b], Alexander Schökel [b], Poul Norby [a]

[a] Department of Energy Conversion and Storage, Technical University of Denmark, Fysikvej 310, Kongens Lyngby, 2800, Denmark
[b] Deutsches Elektronen-Synchrotron DESY, Notkestr. 85, Hamburg, 22607, Germany

ARTICLE INFO

Keywords:
Li-ion battery
Operando X-ray diffraction
Lithium diffusion
18650
Synchrotron radiation

ABSTRACT

Homogeneity in Li-ion battery electrodes is a crucial element in obtaining high performance and long cycle life. In this work inhomogeneities in lithium distribution in NMC cathodes and graphite anodes in cylindrical cells have been tracked in real time during cycling, using operando and ex situ high energy X-ray diffraction. A set of 18650 cells having undergone different cycling protocols and at different stages of degradation have been studied during operation at two different C-rates using synchrotron radiation, scanned along the height of the cells. Significant lithium gradients along the height of the cells have been found, with large changes in inhomogeneity over the course of up to 11 charge/discharge cycles performed operando. Lithium inhomogeneity has been found to be different in cathodes and anodes, and depend heavily on degradation state, state of charge, C-rate, and relaxation steps. Phase relaxation during OCV was quantified, such that after charge $LiC_6 + LiC_{18} + C \rightarrow LiC_{12}$, and after discharge $LiC_{12} + C \rightarrow LiC_{18}$.

1. Introduction

Battery performance and degradation is linked to a large number of factors. Internal factors such as structural change in electrode active materials, electrolyte and electrolyte additives, formation cycles, the cycling protocol followed and more all impact the long term stability of lithium-ion (Li-ion) cells [1–3]. In addition to these, intrinsic factors such as the geometry of the cell, stack pressure and current collector placement can lead cells to exhibit inhomogeneities in lithiation during operation. Inhomogeneities occur both on a micro level and a macro level. On the particle level, lithium gradients within individual oxide particle have been investigated [4], and on the local electrode level inhomogeneities within the electrode thickness also affects performance [5]. On a macro level, significant inhomogeneities across electrodes lead to areas that are more active than others, with these areas then experiencing a higher effective cycling rate exacerbating other degradation mechanisms and potentially leading to failure.

The global market for 18 650 cylindrical cells was valued at 6.34 billion $ in 2020, and is forecast to reach 7.09 B$ in 2027 [6]. 18 650 cells are ubiquitous in consumer electronics, power tools, and used on a large scale in Tesla electric vehicles (EV). The shift towards larger cylindrical cells such as 21 700 cells import many of the same geometrical constraints from 18 650 cells, and thus degradation mechanisms linked specifically to the cylindrical cell format are well worth investigating and understanding.

Macro scale inhomogeneity in lithiation across electrodes in different formats of battery cells can be investigated ex situ by extracting electrodes from cells at different states of health (SOH) and states of charge (SOC), and mapping lithiation using various experimental techniques. There have been previous operando studies using both neutrons and X-rays on 18 650 cells, where a single area of the cell was investigated, with the focus on following structural changes in the active materials [7].

Inhomogeneities in large format cells in commercial formats has been done on both pouch cells and 18 650 cylindrical cells. Most of these studies have been done at open circuit voltage (OCV), with the cell at a fixed state of charge (SOC), with the focus on obtaining high resolution 3D information on lithium (Li) distribution in either cathodes or anodes. In pouch cells, a combination of neutron studies and X-ray studies have shown that inhomogeneities across electrodes in multilayer pouch cells are not entirely predictable, with hot spots appearing in unexpected areas [8]. Inhomogeneity increases with cycling rate. Over time, aged cells seem to remain most active along the edges of the pouch cells [9–12]. In 18 650 cells, inhomogeneities are related to the distance from the centre of the cell roll, as well as vertical position along the length of the cylinder. A combination of diffraction,

* Corresponding author.
E-mail addresses: kvisgr@dtu.dk (K.V. Graae), lixiu@dtu.dk (X. Li), martin.etter@desy.de (M. Etter), alexander.schoekel@desy.de (A. Schökel), pnor@dtu.dk (P. Norby).

https://doi.org/10.1016/j.est.2023.109523
Received 15 May 2023; Received in revised form 29 September 2023; Accepted 28 October 2023
Available online 7 November 2023

Table 1
Table showing the cycling protocol of the five investigated cells. Cells A, B and C were pre-cycled, while Cells D and E were pristine. Cells A, B and D were cycled operando during the synchrotron experiment, while cells C and E were disassembled and studied ex situ. SOH is calculated as the percentage of initial discharge capacity remaining after the final discharge. The Charge column (Chg(CC-CV)) shows first the CC charging current, then the CV cut-off current.

Cell	Chg (CC-CV)	Dchg (CC)	Cycles	Initial Q	Final Q	SOH
Cell A	1C–0.1C	2C	112	2345.3	341.7	15%
Cell B	0.5C–0.05C	2C	141	2476.3	2411.6	97%
Cell C	1C–0.1C	2C	105	2424.3	478.6	20%
Cell D		0.1C				
Cell E		0.1C				

X-ray radiography, as well as X-ray and neutron diffraction tomography techniques have been used to investigate this [5,13–16].

An aspect that has been less investigated is introducing a time-resolved aspect to these studies of spatial inhomogeneity. Charalambous et al. [8] have done time resolved studies on pouch cells at different cycle rates, but limited to three different measurement points along the cell. We have recently done an operando study on 5 Ah pouch cells where 610 points were measured repeatedly using 1 s exposure, resulting in a time resolution of 12 min, enabling inhomogeneity in lithiation across cathode and anode to be followed for pristine and aged cells. The low time resolution however limited the study to 0.2C cycling [9]. A possible approach to remedy this is to limit investigation to a single dimension, as was done with in situ Zn-air cells, where the height of an anode was scanned continuously during cycling [17,18]. The same approach is used here, where we focus on understanding the inhomogeneity along the length of the 18 650 cell, by scanning the centre of the cell during operation, thus providing a high resolution mapping of inhomogeneity in 1D during the full charge cycle, and not only at single time intervals. This study is thus a valuable addition to previous studies done at equilibrium, as the additional information provided by tracking lithiation over the full height of an 18 650 cell in both the cathode and the anode will give good insights into the dynamic lithium diffusion mechanisms during cycling and subsequent OCV steps. This is done on three identical cells having followed different cycling protocols, and it is done at two C-rates. To validate the extent of inhomogeneity along the length and height of the electrode, ex situ mapping of an aged and a pristine cathode has been done as well. To be able to collect high-quality quantifiable X-ray diffraction (XRD) data on 18 650 cells, a high energy X-ray source was essential.

2. Experimental methods

2.1. Sample preparation

Five Samsung ICR18650-26F cells were cycled following the protocols shown in Table 1. The full datasheet from the cell manufacturer is included as supplemental materials. They were cycled between 112 and 141 times at room temperature using a Neware BTS4000 battery cycler, using a constant current (CC) step followed by a constant voltage (CV) step, held until the current reached 10% of the CC current. They were then discharged at CC. The two cells that were disassembled prior to ex situ experiments were discharged to 2.6 V at 0.1C.

One fresh cell (cell E) and one degraded cell (cell C) were disassembled in an argon filled glovebox in a fully discharged state, taking care not to short-circuit the electrodes. Remaining electrolyte was rinsed off in dimethyl-carbonate. The aged $Li_{1-x}Ni_yMn_zCo_{1-y-z}O_2$ (NMC) cathode (57 mm high and 635 mm long) was cut into three pieces of equal length, and sealed in Kapton film. Five pieces were cut from the fresh electrode at 0–40 mm, 146–200 mm, 300–353 mm, 469–500 mm, and 600–635 mm, in order to conserve beam time in the expectation that only limited inhomogeneity would be measured in the fresh electrode.

2.2. X-ray diffraction

All XRD experiments were done at the P02.1 beamline at PETRA III, DESY [19], using a monochromatic wavelength of 0.20733 Å, selected using a double Laue crystal diamond(111)/Si(111) monochromator. The beamline was chosen specifically for its high energy, enabling the beam to penetrate the highly absorbing 18 650 cells. The high flux of 4×10^{10} photons s^{-1} made the operando experiment with a scanning of the cell possible, alongside a sample stage with a rapid motor. The beam size was 1×1 mm^2. Diffraction patterns were collected using a Varex XRD 4343CT (150×150 μm^2 pixel size, 2880×2880 pixel area). The sample-detector distance was 1700 mm, and was calibrated using a LaB_6 sample mounted in a capillary.

The four pieces of electrode wrapped in Kapton (three sections of 22 cm from cell C, and one with all five sections cut from cell E) were mounted in a 3D printed sample holder, and a raster scan of both NMC electrodes was done with 1 mm steps in y and 2 mm steps in x, with an exposure time of 2 s per pixel and with a beam size of 1×1 mm^2. The setup is shown in Fig. 1c.

For operando measurements, the 18 650 cells were mounted vertically in a sample holder as pictured in Fig. 1b, with the 1×1 mm^2 beam hitting the centre of the cylindrical cell. The sample stage was then moved up through the beam in steps of 1 mm for the 0.2C cycles, and 5.5 mm steps during the 1C cycles. Exposure time at each point was 10 s, with a full scan of the cell at 0.2C taking 13 min, and at 1C taking 1 min. A dark exposure was taken at the end of each scan while the motor moved the sample back to the starting position. There is no central pin in the cells, so measuring along the centre of the cell did not add additional absorption.

During the operando experiment, the cells were cycled at constant current (CC) using a Biologic SP-300 potentiostat with a 10 A booster, between 2.75 V and 4.2 V, at either 0.2C or 1C, calculated from the nominal capacity of the cells of 2.6 Ah. Beam damage from exposing the cells to X-rays during prolonged cycling is not expected to be a problem. Firstly the beam is scanned along the cell, meaning that every spot on the cell was only exposed for 10 s every 13 min. Furthermore the use of high energy X-rays minimises the interaction of the beam with the exposed sample, minimising the expected beam damage.

2.3. Data analysis

The obtained 2D XRD data were reduced and integrated using Diamond Dawn software [20,21]. The data were then Rietveld refined using Topas Academic (TA) 6.0 [22], and its batch refinement tool, to sequentially refine all data for each cell from a single input file. For the ex situ electrodes, the scale factor and lattice parameter for Al were held constant for both electrodes since they are from identical cells, ensuring a direct comparison. Likewise Cu, Al and Fe lattice parameters were held constant across all three cells cycled operando. The thick cylindrical 18 650 cells generated two broad reflections, since the sample is cylindrical with two walls and a hollow centre, and therefore two diffraction centres. The Fe reflections originating in the steel casing are well defined with 18 mm between them, while the other two diffraction centres are ill defined and result in two broad peaks overlapping. The displacement between those two centres was refined within limits, and is about half the thickness of the cell. Fig. 2 shows the raw diffractograms from an 18 650 cell (cell D) and an extracted cathode (from cell E) (see Table 1). Both are in a discharged state, and from pristine cells. Here the broad split peaks from the 18 650 cell are clearly visible, particularly for the peaks where several reflections do not overlap. A correction can be applied by treating the signal as if it comes from two parallel walls. Scarlet et al. have made a correction for diffraction from capillary walls in a setup with a constant sample-detector distance [23]. Their correction has been adapted for

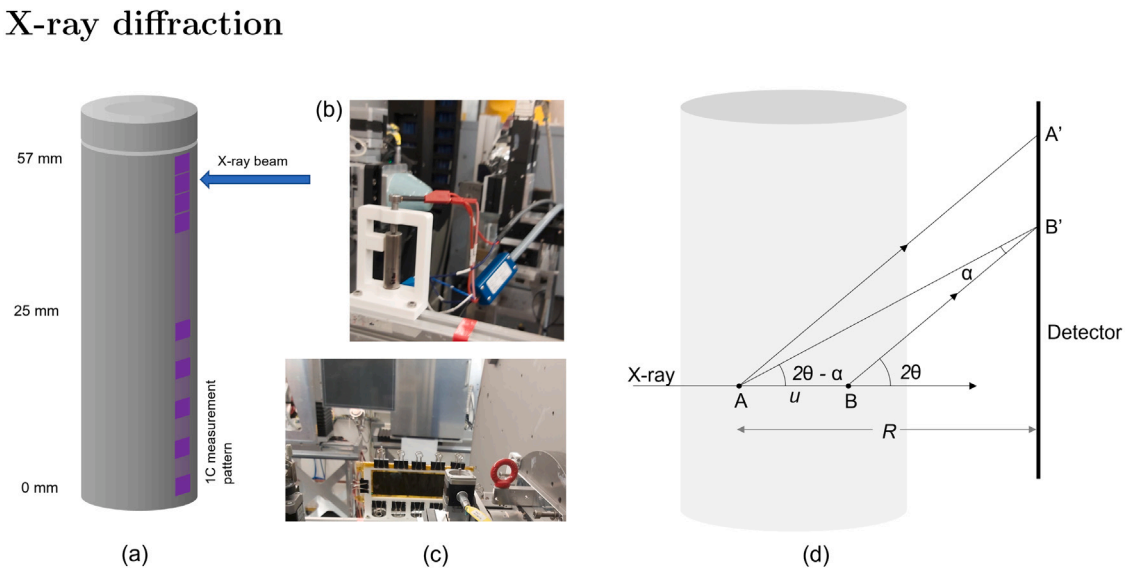

Fig. 1. (a) Scheme of operando experiment along the height of an 18 650 cell. (b) Experimental setup for operando measurements, with an 18 650 cell mounted in a 3D printed frame. (c) A section of the aged electrode wrapped in Kapton and mounted on the sample holder, with the 2D area detector in the background. More images of this setup, alongside a schematic illustration of how the electrode was cut up before being mounted in the frame, are shown in supplemental information. (d) Scheme showing the diffraction geometry resulting in split peaks due to the two diffraction centres A and B in the cell. The distance u between diffraction centres results in the angular shift α. The correction to take this into account is shown in Eq. (2).

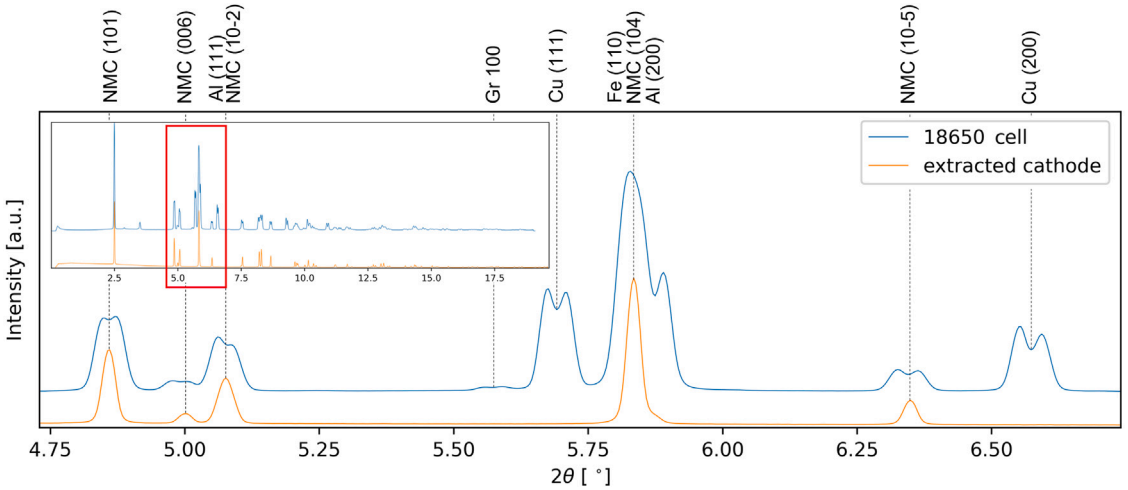

Fig. 2. Selected diffraction peaks from a diffractogram of an 18 650 cell (cell D) and an extracted cathode (from cell E), both in a discharged state and from pristine cells. The insert shows the full diffraction pattern.

this experiment, with the flat detector geometry shown in Fig. 1d, such that the α offset in 2θ is given by

$$\sin\alpha = \frac{u}{R}\sin 2\theta \cdot \cos(2\theta - \alpha), \tag{1}$$

where u is the horizontal displacement and R is the distance to the detector. Since $\alpha \ll 2\theta$ the expression can be approximated to

$$\sin\alpha = \frac{u}{R}\sin 2\theta \cdot \cos 2\theta. \tag{2}$$

While cycling a battery cell with an NMC cathode, the Li occupancy in the NMC crystal undergoes changes. The occupancy is represented as x in $Li_{1-x}Ni_yMn_zCo_{1-y-z}O_2$. Initially at full lithiation, x is around 0.1. As the cell is charged to 4.2 V, x increases to 0.75. Upon complete delithiation of NMC and charging to 4.4 V, x reaches 0.86 [24]. However, it is worth noting that this can vary depending on the precise stoichiometry within the crystal phase. This shift in lithiation has a direct impact on the unit cell parameters a and c in the NMC unit cell, consequently influencing the overall unit cell volume.

Neutron diffraction would allow refinement of the Li-occupancy within the NMC crystal, however obtaining a high spatial and time resolution is challenging, as shown in [9]. An alternative approach to refining Li occupancy is through an estimation based on lattice parameters, which can be done accurately with XRD.

From the Rietveld refinement, lattice parameters for NMC, as well as the phase fractions for the different graphitic phases present in the graphite anode were obtained. The a-parameter for NMC is related to the M-O bond length, which in turn is closely related to the oxidation state and Li-occupancy in the layered oxide structure. Here the NMC a-parameter was used to provide an estimate of x in $Li_{1-x}Ni_yMn_zCo_{1-y-z}O_2$.

During the initial 70% state of charge (SOC), the a-parameter change is close to linear, and is then followed by a more gradual shift. The c-parameter increases with delithiation before eventually collapsing in the fully lithiated state. In this context, the a-parameter has been utilised as a proxy for lithiation, assuming an inverse linear correlation with x. This relationship is described in literature [24].

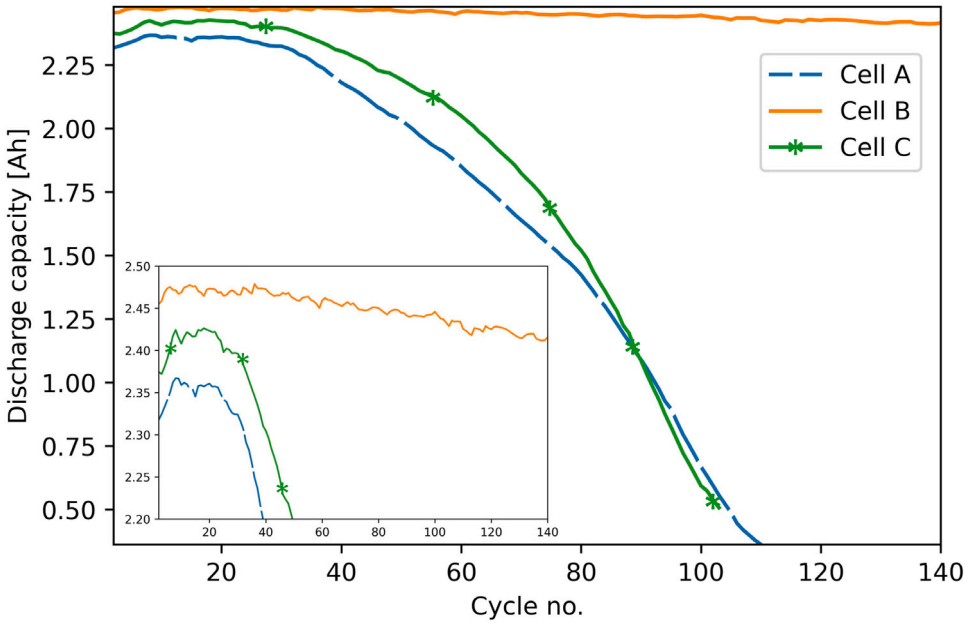

Fig. 3. Discharge capacity for the three cells cycled prior to operando investigation (cell A and cell B), or disassembly and ex situ investigation (cell C (1C charge - 105 cycles)). The insert shows a zoom on discharge capacities between 2.2 Ah and 2.5 Ah, over the same number of cycles. All cells were cycled between cutoff voltages of 2.75 V and 4.2 V. Cell B with charge/discharge currents of 0.5C/2C, and cells A and C with charge/discharge currents of 1C/2C. In both cases a CV step during charge was held until 10% of the charge current was reached.

Since the precise stoichiometry of the NMC cathode in these cells is not known, the potential of a slowly charged and discharged pristine cell is used to define the *a*-parameter corresponding to a lithiation state of $x = 0.1$ and $x = 0.75$ in $Li_{1-x}Ni_yMn_zCo_{1-y-z}O_2$, as described by Marker et al. [24] Using the parameters in cell D, during the operando cycle at 0.2C (Fig. 5(c)), $a = 2.818$ Å has been used to define $x = 0.1$, and $a = 2.870$ Å to define $x = 0.75$. For the graphite anode, the lithiation state is represented as x in Li_xC_6, which is calculated as in [9], i.e. from the relationship between weight percent of the different graphitic phases present in the anode (graphite, LiC_18, LiC_12 and LiC_6). Here LiC_12 and LiC_6 are stoechiometric, while the phase denoted as LiC_18 goes from pure graphite to stoechiometric LiC_18, and is characterised by an evolution in the c-parameter. A detailed description is provided in the authors' previous paper [9].

3. Results and discussion

3.1. Electrochemical performance

Five identical 18 650 cells were investigated, of which three were cycled, and two were kept in a discharged state. The four different test protocols are shown in Table 1. The nominal capacity for all cells is 2600 mAh. The measured initial capacities rose during the first few cycles and peaked at 2345 mAh, 2476 mAh and 2424 mAh. The discharge capacities are shown in Fig. 3.

All cells were charged with a constant current (CC) followed by a constant voltage step (CV), and discharged at CC. The maximum charge current recommended by the manufacturer is 2.6 A (1C), with the recommended charge current being 1.3 A. The maximum recommended discharge current is 5.2 A (2C). The cycle life disclosed by the manufacturer is a capacity retention of 70% (>1.785 Ah) after 299 cycles at the standard cycling regime of 1.3 A charge to 4.2 V with a CV step to 0.05C and a 1.3 A discharge at CC with at 2.75 V cutoff. Cell A (1C charge - 112 cycles)and cell C (1C charge - 105 cycles) were charged at 1C, while cell B (0.5C charge - 141 cycles) was charged at 0.5C. All cells were discharged at 2C. The 1C charge rate had a heavy impact on the degradation of cells A and C, with the cells losing 85% and 80% of their initial capacity after only 112 and 105 cycles. They did however recover most of that lost capacity when cycled slowly at the end of the cycle test, with a resulting discharge capacity of 1920.8 mAh (82% SOH) and 2004.2 mAh (83% SOH). Cell B (0.5C charge - 141 cycles) lost 1.9% per 100 cycles. The very fast failure of these cells was unexpected, given that they were cycled within the limits set by the manufacturer. The rationale of cycling the cells at the maximum recommended charge and discharge rates was in the expectation that only heavily degraded cells would show clear lithium inhomogeneities.

High energy XRD was performed on discharged cathodes, extracted from Cell C (1C charge - 105 cycles) and Cell D (pristine). This enabled a loss of intercalated Li to be quantified, by using the *a*-parameter for NMC as a proxy for lithiation. Using high energy XRD three cell were cycled operando, while the cells were scanned lengthwise as illustrated in Fig. 1, to probe vertical inhomogeneities in Li distribution.

3.2. Electrodes measured ex situ

Fig. 4 shows a detailed 2D map of Li distribution in the NMC cathode of cell E (pristine) (top) and cell C (1C charge - 105 cycles) (bottom), shown as x in $Li_{1-x}Ni_yMn_zCo_{1-y-z}O_2$. It is immediately clear that there are large heterogeneities in Li across the cathode, with large areas nearly completely delithiated, despite the electrode being fully discharged.

The pristine electrode (Fig. 4a) displays no vertical inhomogeneity, while the centre of the electrode roll (leftmost part of the electrode shown in Fig. 4) is more lithiated than the outer edge of the roll by $\Delta x = 0.2$. The innermost part of the electrode is thus less lithiated from the onset, indicating that the tightly rolled centre of the cell may limit lithium diffusion. This has previously been found to be the case for fresh graphite anodes in 18 650 cells [14,25], and the geometrical constraints leading to low lithiation in charged (lithiated) anodes could well lead to low lithiation in discharged (lithiated) cathodes as well. Only portions of the pristine cathode were scanned, in the interest of conserving beamtime, and in the expectations that no large inhomogeneities would be seen.

The aged electrode (Fig. 4b) is in contrast heavily heterogeneous in lithiation. The colour scale shows x from 0.1 to 0.75, so the red areas on the heatmap in Fig. 4 are nearly fully delithiated, and the

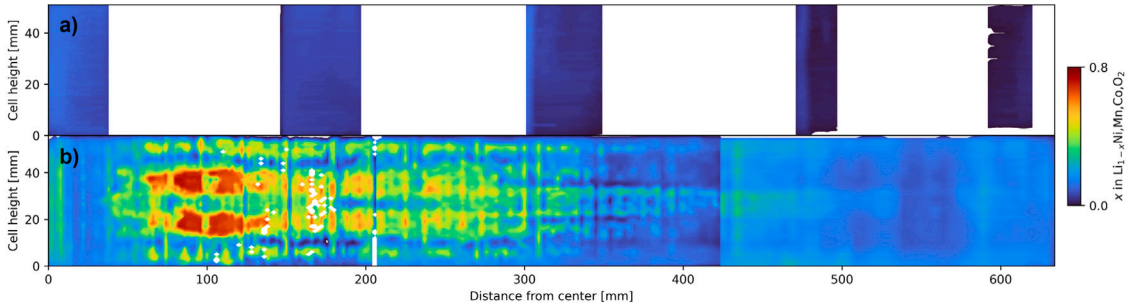

Fig. 4. Cathodes extracted from the pristine cell E (a) and the aged cell C (b). Both cells were discharged to 2.6 V at 0.1C before disassembly, and care was taken to avoid short-circuiting the electrodes. Here x in $Li_{1-x}Ni_yMn_zCo_{1-y-z}O_2$ is shown as a function of position. The full cathode for cell C is shown (b), while only selected sections of the cathode from cell E (a) are shown. (Only portions of the pristine cathode were scanned, in the interest of conserving beamtime.) A schematic illustration and images of the experimental setup are shown in supplemental information. (For interpretation of the references to colour in this figure legend, the reader is referred to the web version of this article.)

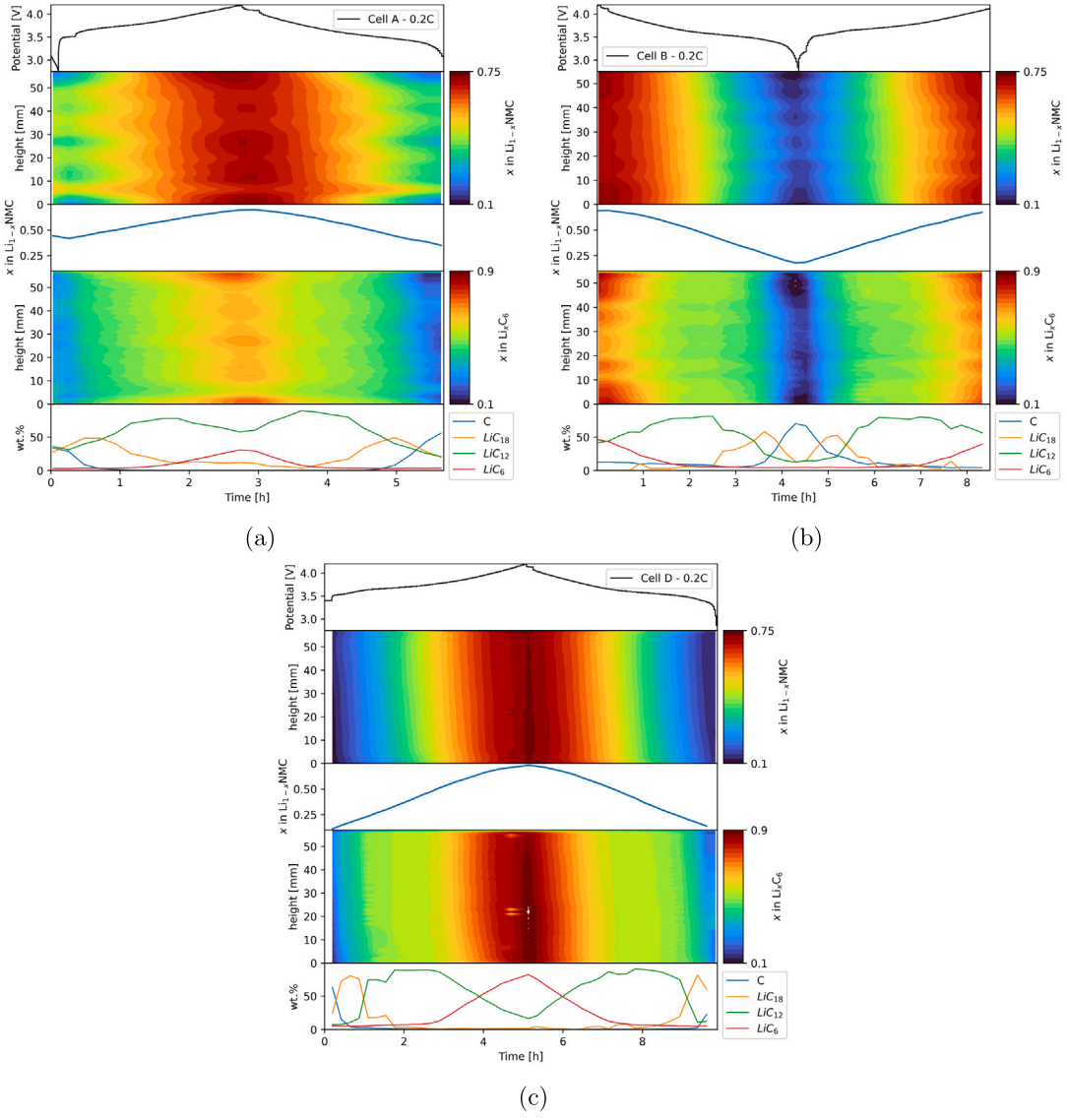

Fig. 5. Cells cycled at a 0.2C rate at constant current, with x in $Li_{1-x}Ni_yMn_zCo_{1-y-z}O_2$ and x in Li_xC_6 for the full height of the cell as a function of time shown as heatmaps. x in $Li_{1-x}Ni_yMn_zCo_{1-y-z}O_2$ and the wt.% of graphite phases are shown as line plots. (a) Cell A, (b) cell B and (c) cell D. Cell B begins with a discharge, followed by a charge cycle.

extensive green areas are only slightly more than half lithiated. The average lithiation across the whole electrode is $x = 0.32$. Taking into account the fact that the anode/cathode capacity ratio is probably 1.1, this matches the remaining 83% SOH in the slowly discharged cell C (1C charge - 105 cycles). There is a distinctive y and x component to the inhomogeneity. Along the cell height the most degraded areas are not completely in the centre of the cell, but offset at around 1/3 and 2/3 of the cell height, as well as at the outer edges of the cell. Along the length of the electrode, the centre is clearly more degraded than the outer layers of the electrode roll. Interestingly the very centre, i.e. the most tightly wound part, is not the most degraded, with the inner 30 mm being at around $x = 0.25$. The worst affected area is from around 80 mm to 300 mm. This is consistent with anode behaviour shown by spatially-resolved time-of-flight neutron diffraction studies of 18 650 cells [14], as well as X-ray attenuation studies [25], where the most heavily degraded parts of the cell are around a third out on the electrode. This confirms that the behaviour is similar in cathodes. Two possible explanations could be: (1) Since the very centre of the cell experiences the lowest Li diffusion, illustrated by the lower lithiation in the centre of the pristine cell (Fig. 4, upper panel), it may also be less heavily cycled, with the local SOC being limited during both charge and discharge, to the detriment of other areas of the cell, that then operate at a higher effective C-rate. (2) There is evidence that the electrolyte concentration in aged cells is generally lower in the centre of the cell, but with a small pocket of electrolyte along the centre of the cell [15]. This would benefit the cathode in this centre area, as well as in the outermost part of the electrode, permitting ongoing electrochemical activity. The previous work by Mühlbauer et al. [15] focuses on the effect this has on graphite lithiation, but it is clear from these results that this also heavily affects the cathode.

In the outermost section of the electrode, from around 400 mm to 620 mm, vertical inhomogeneities are most pronounced along a central band about 12 mm wide. To get a better understanding of these vertical inhomogeneities, three cells have been cycled, while XRD was sampled along the y-axis (Fig. 1), yielding operando 1D resolved data.

3.3. Inhomogeneity in Li distribution along cell height - slow cycling

Cell A, Cell B (0.5C charge - 141 cycles) and Cell D (pristine) were cycled operando, with discharge capacities during the operando cycle of 1406 mAh, 2221 mAh and 2419 mAh, so 60% SOH, 90% SOH and 100% SOH. Cell D, in its pristine state (Fig. 5(c)), is homogeneously lithiated throughout the full cycle, and serves as a good benchmark to compare with the other cells. As was apparent with the ex situ data on discharged electrodes (Fig. 4a) there is little visible lengthwise heterogeneity. The cell achieves its nominal capacity, and the bottom frame in Fig. 5(c) shows that the graphite is more than 90% lithiated, with LiC_6 being the dominant phase. It therefore makes sense to assume that the NMC cathode is also operating in the full range of $0.1 < x < 0.75$ when cycled between 2.75 V and 4.2 V. The NMC a-parameter in the charged and discharged state for cell D (pristine) has thus been used to define the lithiation state of the other cells, assuming a linear relationship between lithiation state in the NMC structure, and the a-parameter (the relationship is in reality not fully linear at low lithiation, as can be seen in the third frame in Fig. 5(c)).

Cell B (0.5C charge - 141 cycles) (Fig. 5(b)), cycled operando in the beam after 141 cycles and reaching a SOH of 97%, shows significant lengthwise inhomogeneity compared to the pristine cell D, with striped patterns of differing lithiation visible on both electrodes. Similar to the pattern seen on the discharged cathode mapped ex situ (Fig. 4), this inhomogeneity is concentrated around a central band between 20 mm and 30 mm, in a narrower band at 10 mm and 40 mm, and along the outer extremities at the top and bottom of the electrode roll. The inhomogeneity on the anode side is more pronounced than on the cathode side, with a lateral range in the charged state of $\Delta x = 0.2$, compared to $\Delta x = 0.1$ for the cathode, as seen in Fig. 6. On the cathode side the line plot of x (Fig. 5(b), third frame) shows that the cathode is fully delithiated in the charged state, but is not fully lithiated again when discharged, while the plot of graphite phase fractions in the bottom frame (Fig. 5(b)) shows that when fully charged, there are equal amounts of LiC_12 and LiC_6 present, so the graphite anode is less lithiated than in the pristine cell D. Graphite is still fully delithiated in some regions when the cell is discharged (apparent from the Li_xC_6 heatmap, Fig. 5(b)), but with some inhomogeneity.

Cell A (1C charge - 112 cycles) was cycled at a higher C-rate prior to the operando experiment (Table 1), with the higher 1C charge rate contributing to a final SOH of 15%. The cell recovered to 82% SOH after a slow cycle, showing that the kinetics of Li diffusion in the cell were severely hampered, but that most of the Li inventory was still accessible at low C-rates. The inhomogeneity in Li along cell height is more pronounced than in cells B and D, with the range in the cathode being about $\Delta x = 0.3$ when discharged, a threefold increase compared to cell B (0.5C charge - 141 cycles)(Fig. 6(a)). Slow Li diffusion is concentrated along bands similar to cell B (0.5C charge - 141 cycles), but with less emphasis on the central 10 mm band between 20 mm and 30 mm. There is a pronounced inactive area in both electrodes at around 7 mm, which remains largely inactive during the full cycle, remaining within $0.65 < x < 0.7$ in NMC and $0.55 < x < 0.6$ in graphite, compared to an average range in the whole cell of $0.3 < x < 0.74$ and $0.2 < x < 0.73$ for NMC and graphite. This indicates a near-complete absence of electrochemical activity in this area, in the full thickness of the electrode roll, which would correspond to an inactive band running the full length of the 635 mm electrode in the ex situ measurement in Fig. 4. From x in the NMC line plot (third frame, Fig. 5(a)) it can be seen that NMC can be nearly fully delithiated, but not lithiated, with the capacity limitation at 0.2C being Li inventory. Likewise on the anode side, the wt.% of LiC_6 when fully charged is half of LiC_12. The large capacity drop for graphite stems from a lack of cyclable Li, as is the case in the cathode. Some degradation in the graphite is apparent from the remaining Li when the cell is discharged, indicating that at the applied potential some Li remains inaccessible and intercalated in the anode.

The effect of ageing on the cells cycled at 0.2C can be seen in the differences between cells A, B and D. As discussed in relation to the ex situ measurements, the most pronounced geometrical effects are seen as a function of the position in the electrode roll, with the inner part of the electrodes showing slower Li diffusion and higher degradation. Here only lateral inhomogeneity is distinguished, and the geometrical effects are less obvious. Looking at Fig. 6 it seems that capacity is lost on the anode side before it is lost on the cathode side, as seen by cell B (0.5C charge - 141 cycles)showing significant inhomogeneity and low x in the anode, while the cathode is still quite homogeneously delithiated. In the more degraded cell A, x in the charged anode is not much lower than in cell B (0.5C charge - 141 cycles), but a reduction in cyclable Li inventory is expressed by the high amount of Li remaining in graphite when the cell is discharged, and the correspondingly high x in the cathode, which is also very inhomogeneously distributed.

There are several possible explanations for the increase in heterogeneity in Li across the cell. Inhomogeneous distribution of electrolyte as a result of gravity has been reported in 18 650 cells cycled vertically [15], resulting in less activity on the upper part of the cells. Such a distribution along cell height has not been seen here, neither in ex situ or operando results, so does not seem to be a plausible explanation for the inhomogeneity seen here, and would not explain the distinctive bands of less active areas along the height of the cell.

The process of rolling the electrode/separator stack and inserting it in the cell casing could perhaps introduce some uneven strain patterns, resulting in the inhomogeneous degradation. The placement of the current collector tabs could perhaps result in uneven winding of the roll [25], however in the investigated cells the tabs run the full length of the electrodes, so should result in even strain. There are also reports on pouch cells that show that differing stack pressure has a limited effect on Li diffusion in electrodes [8].

Another explanation could be that rapid charging generates significant heat, with an uneven convection of that heat resulting in the striped inhomogeneity seen along the electrode length and cell height.

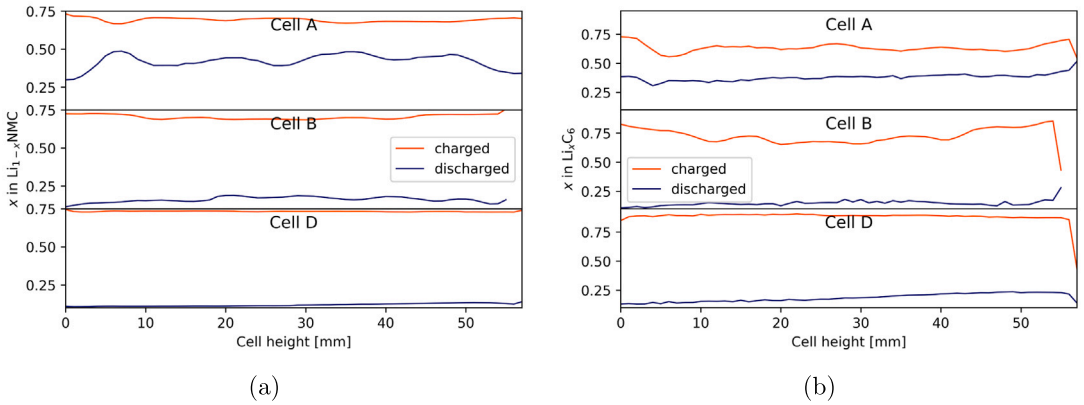

Fig. 6. (a) x in $Li_{1-x}Ni_yMn_zCo_{1-y-z}O_2$ and (b) x in Li_xC_6, plotted as a function of cell height in the charged and discharged state. These lineplots show a snapshot of the 1D variation in x shown as a heatmap in Fig. 5.

3.4. Inhomogeneity in Li distribution along cell height - rapid cycling

Cells A, B and D were all cycled operando at a 1C rate after the 0.2C operando cycles. Cells B and D were cycled a single time, while cell A (1C charge - 112 cycles) was run for 11 cycles, to investigate the rapid reduction in available Li inventory.

In Fig. 7 the first and last cycles for cell A (1C charge - 112 cycles)are shown (Figs. 7(a) and 7(b)) alongside 1C cycles for cell B (Fig. 7(c)) and cell D (pristine) (Fig. 7(d)). The same pattern seen with the slow cycles (Fig. 5) is seen here, with cathode lithiation in cell D (pristine) being homogeneous throughout the cycle despite the increased C-rate, with NMC operating in as wide a x range as at 0.2C (frame 3 in Fig. 7(d)). The bottom 10 mm in the anode seems to be slightly less active than the middle of the cell (top of the heatmap). Cell B (0.5C charge - 141 cycles) is slightly less homogeneous (Fig. 7(d)), with the bottom portion seeming to lead the reaction at the onset of charge, but is also the area that reaches the lowest lithiation for the cathode, and highest lithiation in the anode. The largest inhomogeneity is seen in cell A. Before the first cycle (Fig. 7(a)) the cell does not reach total equilibrium during the OCV step. Once charging begins, the cathode is most active toward the centre of the cell, while the anode is most active in the bottom. This also holds for the tenth cycle (Fig. 7(b)). In both cases, the anode at the bottom is $\Delta x = 0.1$ less lithiated than the middle of the cell, while the cathode is uniformly lithiated within $\Delta x = 0.04$. The middle of the cell reaches its final lithiation state before the bottom edge. In these figures the actual charge and discharge steps are short compared to the OCV steps, with the cell charging between 0.25 and 0.5 h and discharging between 0.75 and 1 h in Fig. 7(a), and charge/discharge between 0.3 and 0.4 h, and 0.68 and 0.78 h in Fig. 7(b), i.e. a total charge duration at 1C taking 15 min (corresponding to 25% SOH) in the first cycle, and 6 min (corresponding to 10% SOH) in the last cycle. As will be shown later, a significant rearrangement of Li in the graphite phases happens during the OCV steps between each cycle step.

The pristine cell D still operates close to the cathode's full lithiation range of $0.1 < x < 0.72$ (Fig. 7(d)). Cell B (0.5C charge - 141 cycles) (Fig. 7(c)) operates in a slightly narrower range of $0.15 < x < 0.66$ on the cathode side, while cell A (1C charge - 112 cycles)is significantly more constrained, with the cathode operating between $0.35 < x < 0.56$ in the first cycle (Fig. 7(a)), and $0.44 < x < 0.52$ in the 10th cycle (Fig. 7(b)). The less degraded cells B and D are most capacity constrained at high x, while the more degraded cell A (1C charge - 112 cycles)is most constrained at low x. This could be attributed to an early degradation and inactivation of the cathode leading to an early rise in overpotential, and thus an initial capacity limitation at high x. Once the cell degrades more heavily, degradation mechanisms affecting the overall Li inventory in the cell take over, which are expressed as a lack of Li to be intercalated in the discharging cathode.

3.5. Relaxation mechanisms during 1C cycling

Cell A (1C charge - 112 cycles) was cycled 11 times operando (Fig. 8), while moving the sample so the beam hit five different positions along the bottom section of the cell. As mentioned earlier, the cell was already heavily degraded, retaining only 15% of its initial capacity after cycling 112 times. Subject to a slow charge cycle however, 82% of the starting capacity was recovered, meaning that the high C-rate caused the cell to operate in a narrow band with limited Li inventory, while most of the Li inventory was still accessible at low currents and lower overpotential. By cycling the cell rapidly operando, it was attempted to reproduce the conditions leading to a rapid fall in capacity. The first operando cycle begins at around 25% of the initial capacity, and the last ends at 10%, so this is indeed achieved. Such a fade rate is realistic compared to the rapid capacity fade seen in Fig. 3, with the additional contributing factor being that no CV step was included in the operando measurement.

3.5.1. Li inventory evolution in the cathode

The third frame in Fig. 8 shows x in $Li_{1-x}Ni_yMn_zCo_{1-y-z}O_2$. Here it is clear that the cathode operates in a rapidly narrowing band. The largest fall in range comes at low x, going from $x = 0.35$ after the first discharge to $x = 0.42$, while at high x it goes from $x = 0.55$ to $x = 0.52$, meaning that the amount of active Li^+ ions falls drastically as the kinetics worsen. During the charged OCV steps from the third cycle onward, the NMC cathode regains Li^+ after the current stops being a driving force. This is not directly reflected in a rise in the anode (fifth frame in Fig. 8). During OCV in the discharged step however, there is again a fall in x in $Li_{1-x}Ni_yMn_zCo_{1-y-z}O_2$, which is directly matched by a rise in x in Li_xC_6 in the anode, and a subsequent lithiation of some of the graphite phase (bottom frame in Fig. 8). This pattern persists during all the observed cycles.

3.5.2. Rearrangement of graphite phases during OCV

Observing the relative phase fractions of the graphite phases in the bottom frame of Fig. 8 the role of kinetics in (de)lithiating the anode is visible. Changes in OCV should directly reflect changes in phase composition, as Li reverts to its most favourable position. Observing first the OCV steps after the charge steps, distinguished by the flat x in $Li_{1-x}Ni_yMn_zCo_{1-y-z}O_2$ in the third frame: The OCV steps begin with LiC_6 reaching its highest point, which makes sense since this is the most lithiated state achieved by the graphite anode. Immediately after current drop-off however, the amount of LiC_6 begins falling, alongside the continuing fall in the amount of LiC_18 and graphite. During this, the wt.% of LiC_12 continues to rise rapidly, and continues to do so until just beyond when the cell is beginning to discharge. Once the cell is

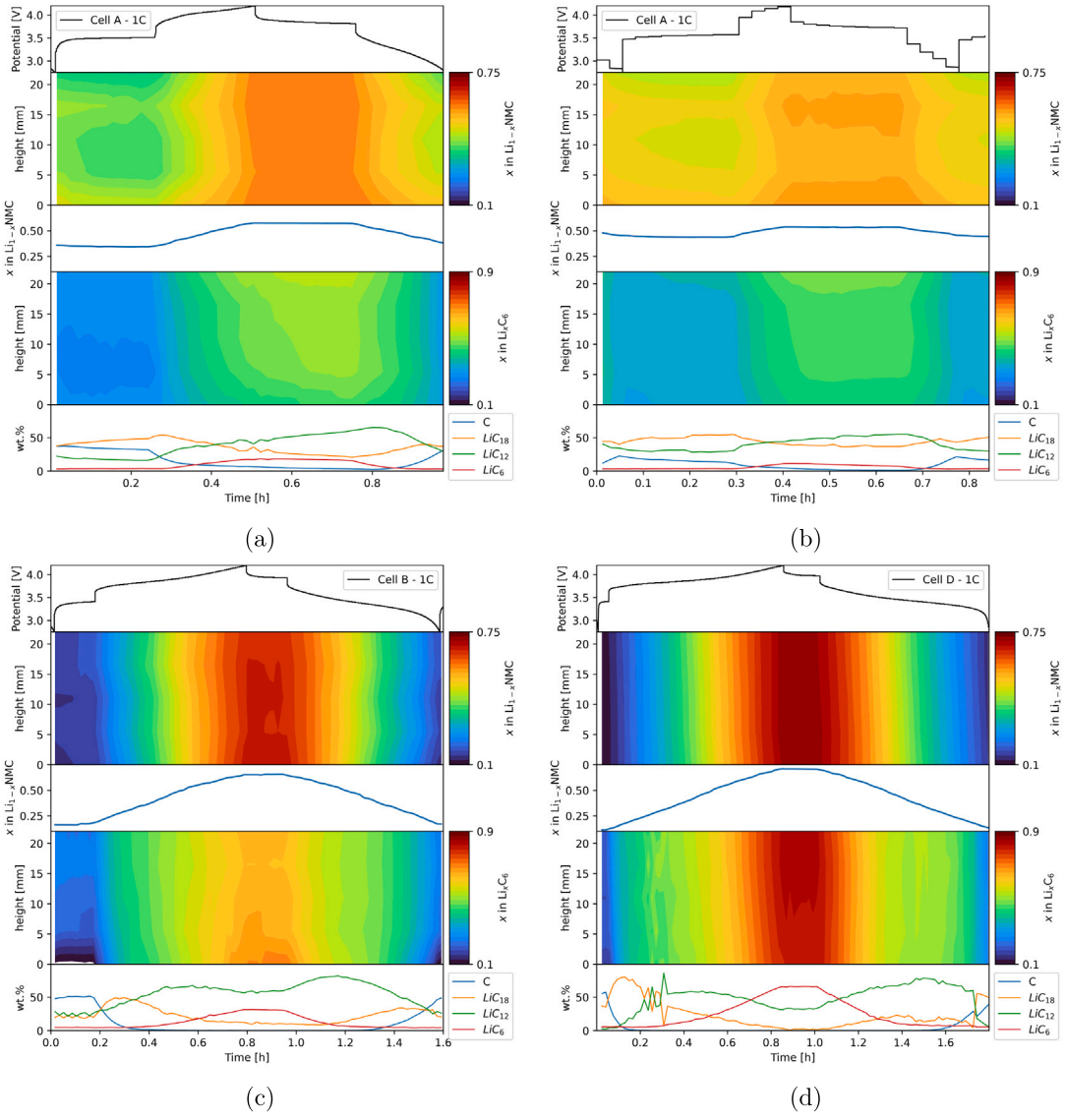

Fig. 7. Cells cycled at a 1C rate at constant current, with x in $Li_{1-x}Ni_yMn_zCo_{1-y-z}O_2$ and x in Li_xC_6 shown as heatmaps for the bottom half of the cell, as a function of time. x in $Li_{1-x}Ni_yMn_zCo_{1-y-z}O_2$ and the wt.% of graphite phases are shown as line plots. (a) Cell A cycle 1, (b) cell A cycle 10, (c) cell B, (d) cell D.

discharged, the wt.% of LiC_6 falls off as expected, with LiC_12 following closely behind, while LiC_18 and graphite rises. When OCV is once again reached, another interesting phenomena can be observed; OCV begins with the graphite signal at its highest, which is expected since the anode is now in its lowest lithiation state, but as the current stops the graphite signal rapidly falls off, while LiC_18 in turn rises sharply. LiC_12 benefited from rearrangement of Li^+ when charged, but during discharge the LiC_12 wt.% falls off too during this OCV step. These trends continue for the full 11 cycles.

From these results, the relaxation of the anode into the most optimal graphitic phases can be directly observed. When charged, the overall lithiation of graphite is around $x = 0.5$ in Li_xC_6 (fifth frame in Fig. 8), corresponding exactly to the stoichiometry of LiC_12. During the rapid charge, the most accessible parts of the anode are lithiated to a higher degree, contributing to a rise in LiC_6, while a significant part of the anode still contains less Li and remains as LiC_18 or graphite. These areas are however still accessible, albeit less so. During the OCV step Li and graphite is rearranged in their lowest energy state, with most of the anode as LiC_12. As the cell loses capacity over the 9 h experiment, the overall lithiation of the graphite anode when charged falls from $x = 0.5$ to $x = 0.45$ meaning that the lowest energy state is now a combination of LiC_12 and LiC_18. This is visible as a stabilisation of the LiC_18 level, and a slower rise in LiC_12 during the charged OCV steps.

When discharged, the anode reaches $x = 0.25$ in Li_xC_6 (fifth frame in Fig. 8) after the first discharge, and $x = 0.33$ after the last. LiC_24 corresponds to $x = 0.25$ (LiC_24 is seen here as LiC_18) and LiC_18 corresponds to $x = 0.33$. In the first cycles the lowest energy state is thus LiC_24 and in the last cycle the lowest energy state would be LiC_18, but there remains a floor of LiC_6 and LiC_12 present during all the cycles, meaning that LiC_18/LiC_24 levels continue to rise and do not reach equilibrium. Meanwhile graphite wt.% drops off very rapidly, meaning that there are some anode particles that are still very accessible and able to rapidly (de)lithiate, even during the last cycles.

Over the course of the 11 cycles shown in Fig. 8 it thus seems that significant Li diffusion happens in the anode during relaxation, an effect that does not happen to this extent in cell B and D (Figs. 7(c) and 7(d)). This could be attributed to the sluggish kinetics in the anode preventing all active graphite particles from being (de)lithiated simultaneously,

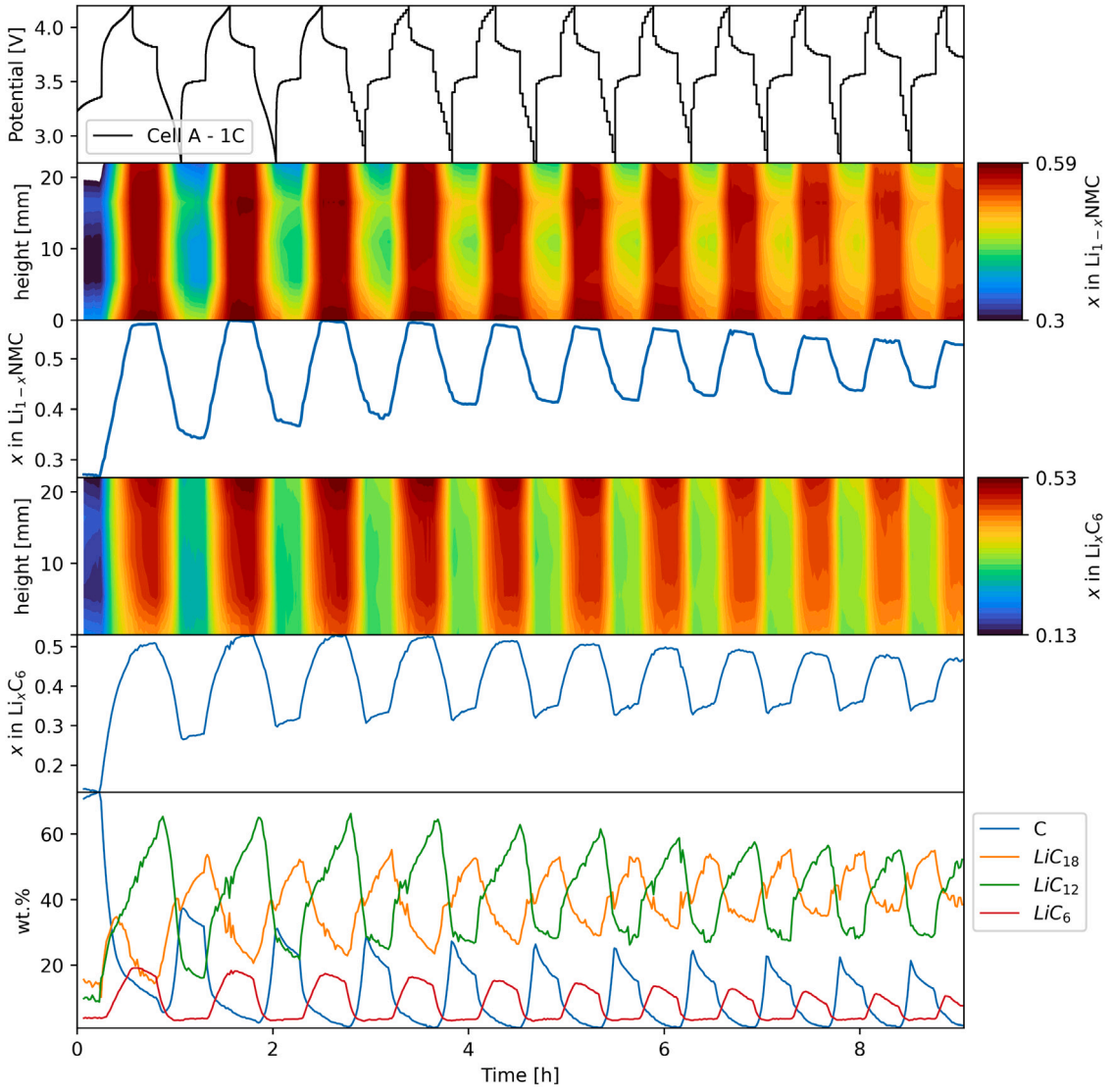

Fig. 8. The aged cell A cycled 11 times at 1C at constant current, with x in $Li_{1-x}Ni_yMn_zCo_{1-y-z}O_2$ and x in Li_xC_6 for the bottom half of the cell as a function of time shown as heatmaps. x in $Li_{1-x}Ni_yMn_zCo_{1-y-z}O_2$, x in Li_xC_6 and the wt.% of graphite phases are shown as line plots. The colour-bars and axes have been re-scaled relative to previous plots to emphasise certain features. (For interpretation of the references to colour in this figure legend, the reader is referred to the web version of this article.)

thus leading to a more pronounced rearrangement of Li^+ ions during OCV.

3.5.3. Spatial relaxation

The heatmaps of the bottom half of the cell shown in Fig. 8 can be used to determine if the relaxation of Li into different graphite phases, or transport from cathode to anode, are also expressed as a spatial migration across the cell, to remedy the inhomogeneities that arise during cycling.

On the cathode side, the bottom seems to be operating at a generally higher SOC than the middle of the cell (top of the heatmap), seen by a higher x when charged, but also a higher x when discharged. The highest lithiation level when discharged (so lowest x) is thus at 20 mm and 10 mm. The areas in between at 15 mm, and the bottom at 0 mm and 5 mm are discharged slower, but are however charged/delithiated at a relatively higher rate. During OCV in the discharged state, Li slowly diffuses into the less lithiated areas at the bottom and at 15 mm, though this happens too slowly for the Li inventory to be homogeneously distributed before the onset of the next charge cycle. The homogeneity improves during charge, and the Li inventory levels out even more out during the subsequent OCV step in the charged state. This could indicate that the lower amount of Li present in the NMC crystal phase when charged allows the remaining Li^+ ions to move around and redistribute more freely. This would also explain the difference in inhomogeneity on the cathode side between charge and discharge at 0.2C in Fig. 6(a), top frame. The inhomogeneity then again increases dramatically during discharge. This pattern continues for all cycles, but with a steadily more inhomogeneous Li distribution, meaning that as capacity is lost the internal diffusion of Li^+ within the cathode slows down. This can also be seen by the wider gaps between contour lines in the heatmaps. The less active areas become more pronounced from cycle 6 onward, and reflect the inhomogeneities also seen in the 0.2C data shown in Fig. 5(a). Here only 5 data points are visible vertically, but the bands along time with less active areas seen in the high-resolution slow cycling data are also evident here.

On the anode side, the spatial effect is even more pronounced than on the cathode, with a larger difference between the bottom and the middle of the cell. In the anode, the middle section (top of the heatmap in the fourth frame in Fig. 8) of the cell is the most lithiated when charged, and also the most delithiated when discharged. The bands of

more and less active areas seen in the cathode are less visible here, with a more direct relationship between the bottom edge and middle of the cell. The inhomogeneity in Li distribution increases fastest when the cell is charged, with lithiation beginning simultaneously along the full height investigated, but with a near-linear gradient in lithiation down through the cell. During OCV after the charge step some of the inhomogeneity is evened out as Li diffuses into lower energy Li phases, and as it diffuses down to graphite particles situated at the bottom of the cell. The discharge step contributes less to an increase in inhomogeneity, as most of the electrode is evenly delithiated. During OCV in the discharged cell there seems to be a delithiation of the middle of the anode (top of the heatmap), coinciding with an overall rise in lithiation shown in the line-plot of x in Li_xC_6 (fifth frame in Fig. 8). Over 10 cycles, the increase in inhomogeneity during the delithiated OCV step increases, and the diffusion of Li^+ contributing to more homogeneous Li distribution in the charged OCV step slows down. These two effects combined lead to a steady increase in overall inhomogeneity as the cell capacity fades.

Spatial redistribution of Li during OCV is a pronounced effect in the degraded cell A. Contrary to the local redistribution of Li within neighbouring graphite particles, a spatial redistribution is also seen during OCV in both cell B and the pristine cell D (Figs. 7(c) and 7(d)). In cell B this happens both in the cathode and in the anode, while in cell D (pristine) it only happens in the anode. This shows two effects related to spatial inhomogeneity; Firstly this shows that spatial inhomogeneities are larger in these cells than local inhomogeneities, and highlights the effect cell geometry has on cell performance. Secondly it indicates that Li diffusion kinetics worsen first in the anode, since spatial inhomogeneity appears in the anode alone in the pristine cell D, while the cathode is still homogeneous.

4. Conclusions

Five commercial 18 650 NMC/graphite cells were investigated using operando and ex situ high energy X-ray diffraction. Two cells at different stages of degradation, along with a pristine cell, were cycled operando while the X-ray beam was scanned along the height of the cell, at both 0.2C and at 1C. This provided unique insights into the time component of significant inhomogeneities in both the cathode and the anode, and their dependency on state of health and cycling rate. To compliment the operando studies of inhomogeneity in 1D, cathodes were recovered from a pristine and a degraded cell. With an ex situ XRD raster scan, an accurate 2D map of lithiation was obtained, quantifying the extent of inhomogeneity in x and y directions.

Li diffusion from the centre to the bottom of the cell was found to be pronounced in even pristine cells, with a redistribution of Li along the y axis happening during OCV. Inhomogeneity in the cathode was found to be two to three times greater in a discharged state than in the charged state. Capacity loss in the graphite anode was found to initially be linked to a loss of Li inventory during charge, and in more degraded cells to contribute to a loss of Li inventory by remaining permanently lithiated when the cell was discharged.

It was found that in the aged cell, Li (de)lithiation of graphite particles is highly inhomogeneous on a local level within a 1×1 mm^2 area, with a significant redistribution of Li^+ to other graphitic particles during open circuit voltage steps. This effect was highly dependent on SOH, and thus not present in pristine cells.

The combination of ex situ and operando observations using high energy X-ray diffraction successfully presents a quantitative insight to degradation mechanisms and lithium heterogeneity under practical cycling conditions.

CRediT authorship contribution statement

Kristoffer Visti Graae: Conceptualization, Experimental work, Data analysis, Writing, Revision. **Xinyu Li:** Experimental work, Data analysis, Revision. **Martin Etter:** Experimental work, Revision. **Alexander Schökel:** Experimental work, Revision. **Poul Norby:** Conceptualization, Experimental work, Revision.

Declaration of competing interest

The authors declare that they have no known competing financial interests or personal relationships that could have appeared to influence the work reported in this paper.

Data availability

Data will be made available on request.

Acknowledgements

We acknowledge DESY (Hamburg, Germany), a member of the Helmholtz Association HGF, for the provision of experimental facilities. Parts of this research were carried out at PETRA III and we would like to thank for use of P02.1. Beamtime was allocated for proposal I-20210738 EC. We thank the Danish Agency for Science, Technology, and Innovation for funding the instrument centre DanScatt. This work was also supported by the Danish Ministry for Higher Education and Science through the SMART Lighthouse.

Appendix A. Supplementary data

Supplementary material related to this article can be found online at https://doi.org/10.1016/j.est.2023.109523.

References

[1] Yaosen Tian, Guobo Zeng, Ann Rutt, Tan Shi, Haegyeom Kim, Jingyang Wang, Julius Koettgen, Yingzhi Sun, Bin Ouyang, Tina Chen, Zhengyan Lun, Ziqin Rong, Kristin Persson, Gerbr Ceder, Promises and challenges of next-generation "beyond Li-ion" batteries for electric vehicles and grid decarbonization, Chem. Rev. 121 (2021) 1623–1669.

[2] Ming Jiang, Dmitri L. Danilov, Rüdiger-A. Eichel, Peter H.L. Notten, A review of degradation mechanisms and recent achievements for Ni-rich cathode-based Li-ion batteries, Adv. Energy Mater. 11 (2021) http://dx.doi.org/10.1002/aenm.202103005.

[3] Jihyeon Kang, Mohamed Atwair, Inho Nam, Chul-Jin Lee, Experimental and numerical investigation on effects of thickness of NCM622 cathode in Li-ion batteries for high energy and power density, Energy 263 (2023) 125801.

[4] John S. Okasinski, Ilyaa A. Shkrob, Marco-Tulio F. Rodrigues, Abhi Raj, Andressa Y.a R. Prado, Andrew C. Chuang, Sarana S. Pidaparthy, Daniel P. Abraham, Time-resolved X-ray operando observations of lithiation gradients across the cathode matrix and individual oxide particles during fast cycling of a Li-ion cell, J. Electrochem. Soc. 168 (2021) 110555.

[5] Pavel Blazek, Peter Westenberger, Simon Erker, Adam Brinek, Tomas Zikmund, Daniel Rettenwander, Nilsa Peter Wagner, Jozef Keckes, Jozef Kaiser, Tomas Kazda, Petr Vyroubal, Martin Macak, Juraj Todt, Axially and radially inhomogeneous swelling in commercial 18650 Li-ion battery cells, J. Energy Storage 52 (2022) 104563.

[6] Global Electric Vehicle Outlook 2022, Tech. Rep., International Energy Agency, 2022.

[7] Qi Liu, Yadong Liu, Fan Yang, Hao He, Xianghui Xiao, Yang Ren, Wenquan Lu, Eric Stach, Jian Xie, Capacity fading mechanism of the commercial 18650 LiFePO4-based lithium-ion batteries: An in situ time-resolved high-energy synchrotron XRD study, ACS Appl. Mater. Interfaces (2018) 4622–4629.

[8] Harry Charalambous, Daniel P. Abraham, Alison R. Dunlop, Stephen E. Trask, Andrew N. Jansen, Tanvir R. Tanim, Parameshwara R. Chinnam, Andrew M. Colclasure, Wenqian Xu, Andrey A. Yakovenko, Olaf J. Borkiewicz, Leighanne C. Gallington, Ut Ruett, Kamila M. Wiaderek, Yang Ren, Revealing causes of macroscale heterogeneity in lithium ion pouch cells via synchrotron X-ray diffraction, J. Power Sources 507 (2021) 230253.

[9] Kristoffer Visti Graae, Xinyu Li, Daniel Risskov Sørensen, Elixabete Ayerbe, Iker Boyano, Denis Sheptyakov, Mads Rya Vogel Jørgensen, Poul Norby, Time and space resolved operando synchrotron X-ray and neutron diffraction study of NMC811/Si–Gr 5 ah pouch cells, J. Power Sources 570 (2023) 232993.

[10] M.J. Mühlbauer, A. Schökel, M. Etter, V. Baran, A. Senyshyn, Probing chemical heterogeneity of Li-ion batteries by in operando high energy X-ray diffraction radiography, J. Power Sources 403 (2018) 49–55.

[11] Monta R. Cosby, Giaa M. Carignan, Zhuo Li, Coreya M. Efaw, Charles C. Dickerson, Liang Yin, Yang Ren, Bin Li, Eric J. Dufek, Peter G. Khalifah, Operando synchrotron studies of inhomogeneity during anode-free plating of Li metal in pouch cell batteries, J. Electrochem. Soc. 169 (2022) 020571.

[12] Volodymyr Baran, Martina J. Mühlbauer, Michael Schulz, Josef Pfanzelt, Anatoliy Senyshyn, In operando studies of rotating prismatic Li-ion batteries using monochromatic wide-angle neutron diffraction, J. Energy Storage 24 (2019) 100772.

[13] Lu Cai, Ke An, Zhili Feng, Chengdu Liang, Stephena J. Harris, In-situ observation of inhomogeneous degradation in large format Li-ion cells by neutron diffraction, J. Power Sources 236 (2013) 163–168.

[14] D. Petz, M.J. Mühlbauer, V. Baran, M. Frost, A. Schökel, C. Paulmann, Y. Chen, D. Garcés, A. Senyshyn, Lithium heterogeneities in cylinder-type Li-ion batteries – fatigue induced by cycling, J. Power Sources 448 (2020) 227466.

[15] M.J. Mühlbauer, D. Petz, V. Baran, O. Dolotko, M. Hofmann, R. Kostecki, A. Senyshyn, Inhomogeneous distribution of lithium and electrolyte in aged Li-ion cylindrical cells, J. Power Sources 475 (2020) 228690.

[16] Gerarda S. Mattei, Zhuo Li, Adama A. Corrao, Chaojiang Niu, Yulun Zhang, Boryann Liaw, Charlesa C. Dickerson, Jie Xiao, Erica J. Dufek, Petera G. Khalifah, High-energy lateral mapping (HELM) studies of inhomogeneity and failure mechanisms in NMC622/Li pouch cells, Chem. Mater. 33 (2021) 2378–2386.

[17] Mathias K. Christensen, Jette Katja Mathiesen, Søren Bredmose Simonsen, Poul Norby, Transformation and migration in secondary zinc–air batteries studied by *in situ* synchrotron X-ray diffraction and X-ray tomography, J. Mater. Chem. A 7 (2019) 6459–6466.

[18] Kristoffer Visti Graae, Poul Norby, Time- and space-resolved in situ X-ray diffraction study of phase transformations and redistribution in Zn–air battery anodes, ACS Appl. Energy Mater. 5 (2022) 11392–11401.

[19] Ann-Christin Dippel, Hanns-Peter Liermann, Jana Torben Delitz, Peter Walter, Horst Schulte-Schrepping, Olivera H. Seeck, Hermann Franz, Beamline p02.1 at PETRA III for high-resolution and high-energy powder diffraction, J. Synchrotron Radiat. 22 (2015) 675–687.

[20] Jacob Filik, Aluna W. Ashton, Peter C.a Y. Chang, Processing two-dimensional X-ray diffraction and small-angle scattering, J. Appl. Crystallogr. 50 (2017) 959–966.

[21] Mark Basham, Jacob Filik, Michaela T. Wharmby, Peter C.a Y. Chang, Baha Ela Kassaby, Matthew Gerring, Jun Aishima, Karl Levik, Bill C.a A. Pulford, Irakli Sikharulidze, Duncan Sneddon, Matthew Webber, Sarnjeeta S. Dhesi, Francesco Maccherozzi, Olof Svensson, Sandor Brockhauser, Gabor Náray, Aluna W. Ashton, *Data* analysis WorkbeNch (*DAWN*), J. Synchrotron Radiat. 22 (2015) 853–858.

[22] Alana A. Coelho, TOPAS and TOPAS-academic: an optimization program integrating computer algebra and crystallographic objects written in c++, J. Appl. Crystallogr. 51 (2018) 210–218.

[23] Nicola Viviennea Yorke Scarlett, Matthewa R. Rowles, Kiaa S. Wallwork, Iana C. Madsen, Sample-displacement correction for whole-pattern profile fitting of powder diffraction data collected in capillary geometry, J. Appl. Crystallogr. 44 (2011) 60–64.

[24] Katharina Märker, Philipa J. Reeves, Chao Xu, Kenta J. Griffith, Clarea P. Grey, Evolution of structure and lithium dynamics in $LiNi_{0.8}Mn_{0.1}Co_{0.1}O_2$ (NMC811) cathodes during electrochemical cycling, Chem. Mater. 31 (2019) 2545–2554.

[25] A. Senyshyn, M.a J. Mühlbauer, O. Dolotko, M. Hofmann, H. Ehrenberg, Homogeneity of lithium distribution in cylinder-type Li-ion batteries, Sci. Rep. 5 (2016) 18380.